IONIZATION AND KINEMATICS OF YELLOW-LINE CORONAL REGIONS

William J. Boardman and Donald E. Billings

Department of Astro-Geophysics
University of Colorado
Boulder, Colorado

ABSTRACT

We compute the ionization of Ca XV from observations of the strengths of the coronal lines λ5694 and λ5446, and the neighboring regions of the continuum. We then compare this with a theoretical ionization curve including dielectronic recombination. Discrepancies are discussed and explanations suggested in the form of turbulence and/or ordered mass motion. Finally we calculate estimates of the dimensions of the observed condensations along the line of sight.

I. Ionization Processes in Calcium XV

The two coronal emission lines at λ5694 and λ5446 occur in extremely hot, active regions of the solar corona (Waldmeier, 1951, 1956; Roberts, 1952). A visual estimate by Waldmeier of the ratio of the intensities of the two lines, I(5694)/I(5446) = 6:1 was pointed out by van de Hulst (1953) to be inconsistent with Shklovsky's (1950) statement that the ratio of the yellow line to its companion should be about 1.5:1. Later, Pecker, Billings, and Roberts (1954), and Zirin (1964), using microphotometer techniques for eliminating the effect of the Fraunhofer spectrum against which the coronal lines are observed, found line intensity ratios ranging

from slightly more than unity to around 3:1, in accord with Shklovsky's predictions. Zirin (1959) implies that there is little doubt that these lines are due to Ca XV at a temperature of about 4×10^6 °K. A certain degree of uncertainty in the temperature remains due to the possibility either of random turbulence or ordered mass motion or both being partially responsible for some of the line broadening. These questions will be considered in detail in a later section.

The ionization curve of any coronal ion depends on temperature only (Woolley and Allen, 1948). The intensity ratios of lines in a multiplet will depend on the electron density, however, since the population of the various levels is determined both by collision and radiative processes. To illustrate this, consider the energy-level diagram shown in Fig. 1. If we consider radiative excitation, the intermediate level may be filled by absorption of a photon of wavelength λ5694; however the population of the upper level from the ground state is impossible by a dipole transition because of the selection rule $\Delta J = 0, \pm 1$. Thus if radiation is the dominant method of excitation, the 5446 line should be comparatively weak. The rates of excitation by electron collision are more nearly equal; consequently for a given radiation field, which we shall assume to be identical for all condensations, the line intensity ratio I(5694)/I(5446) will decrease with increasing electron density, and approach a definite value asymptotically as the collision mechanism of excitation becomes dominant.

The line/continuum intensity ratio for both lines also varies strongly with density. At low densities the upper levels are populated mainly by radiative excitations, whereas at higher densities collision excitation dominates and the line strengths increase strongly (Zirin, 1964).

Zirin (1964) computed the excitation equilibrium of Ca XV for the five lowest states assuming Blaha's (1962) cross-sections for the collisional excitation of the green coronal line to be valid for Ca XV also, when corrected for statistical weights. The results of this calculation show the fraction of Ca XV in the $^3P_2$ and $^3P_1$ states as a function of electron density N_e, and are plotted graphically in Fig. 2. Zirin also computed the line/continuum ratio for each line assuming a Ca/H ratio of 2.5×10^{-6}, and apparently used spontaneous transition probabilities $A_{5694} = 97$ sec^{-1} and $A_{5446} = 83$ sec^{-1}. The expressions for the line/continuum ratios turn out to be:

$$\begin{aligned} I(5694)/I(\text{cont.}) &= 125\ F(^3P_1)\ F(\text{Ca XV}) \\ I(5446)/I(\text{cont.}) &= 106\ F(^3P_2)\ F(\text{Ca XV}) \end{aligned} \qquad (1)$$

where I(line) is in equivalent Ångstroms, I(cont.) is the scattered continuum emission in one Ångstrom, $F(^3P_1)$ and $F(^3P_2)$ are the fractions of Ca XV in the $^3P_1$ and $^3P_2$ levels respectively, and F(Ca XV) is the fraction of Ca existing as Ca XV.

The intensity ratio of the two lines is thus easily determined as a function of the relative population of the two levels, and consequently, as a function of N_e. A plot of the line intensity ratio, R, vs. N_e is given in Fig. 3.

II. Observations

From all the spectrograms taken at Climax near the maximum of the last solar cycle (1956-1960) we chose 11 that had a satisfactory signal-to-noise ratio for intensity and profile measurements. From these we made

microphotometer tracings of each of the yellow lines plus the neighboring continuum. We then shifted the microphotometer slit to a nearby region of the sun's limb away from the emitting region and retraced over the same region of the spectrum. We were thus able to measure both the integrated line intensity and the enhancement of the continuum per 1Å width by overlaying one tracing upon the other in such a way that the photometric standards recorded on each tracing were superimposed (Fig. 4). About 64 wavelength points in the line profiles proper were used in each pair of tracings for the measurement of the radiation enhancement of the active region over the quiet region, thus giving profiles as accurately as film grain would allow. Similar measurements were made of the neighboring continuum enhancement out to about 15Å away from the line on either side. The highly chromatic nature of the coronagraph rendered simultaneous focussing on the two regions impossible so we assumed the actual continuum enhancement was identical in the two regions, and multiplied the line intensity ratio by the inverse continuum ratio as a correction.

Fig. 5 shows the resulting measured values of the line/continuum ratio for both lines as a function of the line intensity ratio. For comparison, Zirin's (1964) theoretical values of the line intensity and line/continuum ratios for the case of F(Ca XV) = 1/5 are plotted. Note from eq. (1) that the curves may be brought into better agreement with our observations if we assume that on the average a slightly smaller value of F(Ca XV) prevails. Considerable scatter also occurs, however, and for the remainder of this paper we shall not assume a constant value of F(Ca XV).

The flow chart in Fig. 6 shows the scheme we used to calculate F(Ca XV) from the measured intensities and Zirin's (1964) theoretical values plotted in Figs. 2 and 3. Measured quantities are enclosed in oblong boxes; computed

quantities or those read from a graph are shown in rectangular boxes.

Table 1 lists the values of I(line)/I(cont.), N_e, $F(^3P_1)$, $F(^3P_2)$, and F(Ca XV) obtained by the method shown schematically in Fig. 6. In addition, the temperatures of the line-emitting regions as inferred from the half-widths of the lines are given. Note the excellent agreement between the calculated values of F(Ca XV) using the two lines (Fig. 7). The linear correlation coefficient of 0.97 is very strong evidence that the two lines arise from the same ion, namely, Ca XV.

The temperatures given in Table 1 were computed from the half-widths of all the lines whose profiles appeared to be reasonably Gaussian in shape. The measurements were made graphically by plotting the measured difference profile of each line and subtracting the average value of the continuum increase in brightness. Fig. 8 shows a plot of F(Ca XV) vs. temperature as calculated by this method. The dashed lines show the extent of the maximum possible uncertainty due to error in the half-width measurements. The probable errors are considerably smaller. A theoretical curve calculated from the ionization equilibrium equations including dielectronic recombination (Burgess, 1965) is also given for comparison. (See Appendix A). Obviously there is a considerable amount of scatter in the points as well as a systematic tendency of the observations to give higher temperatures than those predicted by ionization theory. We shall discuss presently three possible explanations of this tendency, including errors in measurement and/or theory, and motions within the condensation.

III. Errors

The accuracy of F(Ca XV) for the points plotted in Fig. 7 depends on the accuracy of the measurements of the equivalent widths of the lines, and

the continuum enhancement in the line-emitting regions. These measurements were made using a great many wavelength points in the regions of the lines, as described in the preceding section. Significant random errors in measurement are therefore unlikely; however, in some cases the continuum brightness fell to different levels on either side of the portion of the limb containing the condensation. This could either be caused by irregularities in the slit used in the spectrograph, or by real differences in the ambient coronal densities outside the condensations. Therefore, in a few cases it was difficult to specify a reference level for continuum enhancement; we therefore chose the mean brightness on either side of the condensation.

Far more subject to error were the measurements of the half-widths of the lines. The difficulty here arose both from a difference in the continuum brightness on either side of the line in a few cases, and from the presence of some rather strong absorption lines in the wings. This latter difficulty is particularly true of the λ5446 line. A slight misalignment of the two tracings would have a strong effect on the measured profiles, although the line strength measurements would be somewhat less affected. It was found that by constructing the broadest and narrowest profiles imaginable from the points measured on the lines, the greatest resulting temperature difference was never more than 3.2×10^6 °K, with a more typical value being about 10^6 °K (Fig. 8). The probable errors would be considerably less, and in any case are insufficient to explain the degree of systematically high temperatures measured, although they certainly contribute to some of the scatter of the points in Fig. 8 along the temperature axis.

It is also possible that the computed ionization curve, which we obtained using a number of approximate expressions for rate coefficients and oscillator strengths, could be in error. (See Appendix A). To our knowledge, this represents the first computation of the ionization curve of Ca XV in which dielectronic recombination is included. From a comparison of this curve with our observed points we predict that if further refinements alter the ionization curve the change will be in the direction of higher temperatures and higher maximum F(Ca XV).

IV. Random Turbulent Motion

Examination of the profiles of the yellow lines emitted from several condensations show in some cases Doppler shifts of the order of a few tenths of an Ångstrom, and in others, profiles that depart significantly from a Gaussian shape. At this point we shall present a possible interpretation in the form of partially resolved turbulent motion.

If we consider what effects we should expect to arise from observation of line emission through a fairly small number of turbulent cells in the line of sight, we conclude the following: a) that for a smaller number of cells the probability of observing a Doppler shift in the line becomes larger, and b) that if we assume for the moment that the number of cells is fixed, the mean Doppler shift should be proportional to the mean line-of-sight velocity (Billings, 1963).

If for a given observation we let v denote the velocity corresponding to a given line shift; v_i, the velocity of a particular cell; and N, the total number of cells in the condensation, then the observed shift velocity will be roughly equal to the mean velocity, or

$$v^2 = \left(\frac{\sum_i^N v_i}{N} \right)^2 \qquad (2)$$

if we assume the cells are all identical. The effect of turbulence on the broadening of the lines, on the other hand, is the same essentially as that of temperature. We can relate the rms radial velocity V_r and the radial component of the thermal velocity V_{Tr} to the total rms radial velocity V_{HWr} inferred from half-width measurements thus:

$$V_{HWr}^2 = V_{Tr}^2 + V_r^2 \quad . \qquad (3)$$

In terms of our statistical cellular model, however,

$$V_r^2 = \frac{\sum_i^N v_i^2}{N} \qquad (4)$$

by definition.

If we divide (4) by (2), and expand (2) separately into its squared- and cross-terms we find that

$$\frac{V_r^2}{v^2} = N \frac{\sum_i^N v_i^2 + 2 \sum_{i<j}^N v_i v_j}{\sum_i^N v_i^2} \quad . \qquad (5)$$

The sum of the cross-products in the numerator of eq. (5) is an auto-correlation coefficient of the cellular velocities. For random motions, its value rapidly becomes small compared to the sum of the squared terms with an increasing number of terms. Thus we have

$$N = \frac{V_r^2}{v^2} \qquad (6)$$

or, if we wish to consider a typical number of cells obtained from averaging over a number of profiles,

$$\tilde{N} \approx \frac{\overline{v_r^2}}{\overline{v^2}} \qquad (7)$$

to the accuracy of the approximate argument which we have used.

With only two exceptions, all the points lie to the right of the curve in Fig. 8, and except for these two there seems to be little basis for concluding whether the true temperature in any one case corresponds to the ascending or the descending portion of the curve. Undoubtedly we are looking at layers of significantly differing temperatures along the line of sight, since these regions are optically thin and possess steep temperature gradients. Thus any measured temperature is at best only representative, not unique in a given condensation. We therefore decided on two different methods of measuring the turbulent velocities; (1) by measuring each apparent temperature shift from the observed temperature to the point on the ionization curve immediately to the left, and (2) by assuming that all temperatures that will give rise to yellow-line emission are equally probable, and therefore, that on the average the number of cases observed whose temperatures correspond to the ascending portion of the curve should be roughly equal to the number corresponding to the descending portion. We thus selected the half of the points that were closest to the ascending portion and measured the apparent temperature excess for these points from the rising slope. The other points were measured from the descending slope. The points above the curve had the temperature excess measured from the peak of the theoretical curve -- about 3.3×10^6 °K. Henceforth all quantities obtained by methods (1) and (2) will bear these respective numbers as subscripts when the distinction is necessary. Method (1) was selected as establishing the smallest possible velocity and number of cells for turbulent motion; method (2) was selected

as representing a somewhat more plausible state of turbulence. We shall see presently that essentially the same conclusions follow from either assumption.

Table 2 gives the apparent temperature increases ΔT_1 and ΔT_2 and the wavelength shift for each line studied. We used the values λ5694.44 and λ5446.44 for the undisplaced wavelengths (Boardman and Billings, 1965). Note that the shifts are in general considerably larger than the probable error of the values of the undisplaced lines, namely $\pm$ 0.02Å. In each case, the effect of solar rotation on the observed Doppler displacement $\Delta\lambda$ has been compensated for.

From Table 2 we find that $\overline{\Delta T_1} = 1.74 \times 10^6$ °K, and that $\overline{\Delta T_2} = 2.07 \times 10^6$ °K. Thus if $\overline{V_r^2}$ is the mean square turbulent velocity along the line of sight as measured by excess broadening, we may relate $\overline{V_r^2}$ to ΔT thus:

$$\overline{V_{r1}^2} = \frac{1}{3}\overline{V_1^2} = \frac{N_o k}{M}\ \Delta T_1 = 362\ \text{km}^2/\text{sec}^2$$

$$\overline{V_{r2}^2} = \frac{1}{3}\overline{V_2^2} = \frac{N_o k}{M}\ \Delta T_2 = 430\ \text{km}^2/\text{sec}^2\ . \qquad (8)$$

(Here N_o is Avogadro's number, k is Boltzmann's constant, and M is the molar weight of the gas. For Ca, M = 40. Also, $\overline{V^2}$ is the total mean square velocity of the cells as inferred from the temperature excess.)

A computation of the mean square velocity due to the shifts of the lines by the amounts $\Delta\lambda$ in Table 2 gives

$$\overline{v^2} = 66.8\ \text{km}^2/\text{sec}^2\ . \qquad (9)$$

Substitution of (9) into (7) yields the number of cells for each method:

$$N_1 = 5.4 \text{ cells}$$

$$N_2 = 6.4 \text{ cells} \quad . \tag{10}$$

This indicates that a fairly large scale of turbulent motion would be needed to explain the observed Doppler shifts and broadenings. It would appear that at least a fairly substantial portion of the broadening might be explained by random turbulent motions. Additional evidence that turbulence exists may be seen from the rapid variations in the Doppler displacements in both space and time for a given condensation. Note particularly in Table 2 the three tracings made of the spectrogram taken at 20 November 1960 at 2227 UT (labelled 2227II), and also the spectrograms taken on 12 November 1956. The large differences in Doppler shifts measured give evidence of turbulent motion.

Table 3 shows the line-of-sight dimension of each condensation as computed from the electron density and Thomson scattering. (See Appendix B). Note that the ratio in size of the largest to the smallest dimension is considerable greater than the inferred number of cells. Thus if we retain the assumption that all cells are identical we should see on the average, higher Doppler displacements in the smaller regions. This is not observed, and serves as evidence against the turbulent theory, unless we allow the cellular sizes to vary from one condensation to the next.

V. Non-Random Expansion and/or Contraction of Condensations

If we assume that random turbulence occurs within the condensations, then the implied cellular velocities of around 30 km/sec would lead to a characteristic time of random structural changes of about 10 minutes for a condensation of 18,000 km in size, unless the cells are contained in space,

as by a magnetic field. Changes in this order of time have indeed been observed in the form of changing Doppler shifts, as was pointed out in the last section. A time scale of 10 minutes is fairly short, however, compared to the lifetimes of the condensations themselves. The limb flare of 18 December 1956 studied by Zirin (1959) was associated with a hot condensation that showed yellow-line emission at 1822 UT, was still strong at 2226 UT, and faded soon afterward, indicating a time scale on the order of four hours or so. It is evident that once the condensation is formed it is strongly confined to the active region by magnetic fields (Lüst and Zirin, 1960), otherwise we should expect it to dissipate in a time not much greater than 10 minutes. If this is true, then one should expect to find evidence for ordered motion on a somewhat longer time scale than the random turbulence. The brightening of the continuum definitely indicates an increase in density in these regions; this implies in turn a significant flow of matter into these regions at the beginning of the condensation and a dissipation at the end, when the emission fades. Although the characteristic time for the life of the condensation is greater than the same for random motions by a factor of 20 or so, the velocities may be comparable if matter is drawn in to these regions from a sufficiently large volume of the corona.

Figs. 9a and 9b show the intensity of the continuum enhancement near each line observed in units of 10^{-6} times the solar disk intensity plotted against the apparent increases of the line temperatures ΔT_1 and ΔT_2 due to non-thermal broadening. The mean square velocity $\overline{V^2}$ is included on the temperature axes. Although considerable scatter is evident which may be attributed to variation in size and intensity of different active regions, the tendency of a low velocity to be associated with a high density region is

exhibited on both graphs. This is consistent with what we should expect from a large scale expansion and/or contraction, for at maximum density the excursion velocity would be minimal as the minimum volume is approached.

VI. Conclusions

Since the sizes and intensities of the coronal condensations vary considerably, and likewise also undoubtedly other parameters that we have not even considered explicitly such as the magnetic field strength and details of the cellular structure, the scatter in the data we have obtained is not in the least surprising. For this reason we interpreted the data statistically in each case, but additional observational evidence at the next solar cycle maximum will be needed to test our results. We can be certain of substantial non-thermal motion in these condensations, but more exact computations of the theoretical ionization curves might have the effect of decreasing the macroscopic velocities needed to explain the profile broadening, and at the same time increase the sizes of the cells to preserve the observed line displacements.

We also have considered evidence of ordered mass motion. It may be concluded that the observed shifts and broadenings of the lines may be explained by either hypothesis to within the accuracy of our measurements. Evidence of each hypothesis presents itself, however, when sought. It is thus possible that both random and ordered motions exist simultaneously, and it seems quite certain that at least one or the other is operative.

APPENDIX A - Ionization Curves of Calcium

We have computed the theoretical ionization curves of calcium from a collision-ionization rate q as given by Seaton (1962, 1964), a radiative recombination rate α_r by Burgess and Seaton (1964), and a dielectronic recombination rate α_d by Burgess (1965). These expressions are given as quoted by Allen (1965), and are for transitions between ions of charges Z and Z + 1:

$$q = 2.0 \times 10^{-8} (\zeta_Z T^{\frac{1}{2}} I_Z)^2 \, 10^{-5040 I_Z/T} \text{ cm}^3 \text{ sec}^{-1}$$

$$\alpha_{rZ} = 1.3 \times 10^{-9} Z^2 I_Z^{\frac{1}{2}} T^{-1} \text{ cm}^3 \text{ sec}^{-1} \qquad (1A)$$

$$\alpha_{dZ} = 2.0 \times 10^{-4} T^{-3/2} (Z+1)^2 \sum_i f W_{Z+1}^{-\frac{1}{2}} \, 10^{-4600 W_{Z+1}/T} \text{ cm}^3 \text{ sec}^{-1}$$

Here, ζ_Z is the number of electrons in the outer shell, I_Z is the ionization potential in eV from the Z to the Z + 1 ion, W_{Z+1} is the excitation potential in eV of the first optically allowed transition of the recombining ion, and f is the oscillator strength of the same transition. It was found that in general only transitions between levels in the two multiplets of lowest energy needed to be included in the summation in the third of eqs (1A). The necessary multiplet oscillator strengths were obtained from Wiesavsky (1961). Throughout the discussion that follows, we have assumed that the radiation field is sufficiently weak that ionization is produced by ion-electron collision only. In general the equilibrium ratio between the Z and Z + 1 ions is given by

$$\frac{N_{Z+1}}{N_Z} = \frac{q_Z}{\alpha_{rZ} + \alpha_{dZ}} \qquad (2A)$$

By repeated application of (3A) we find the following relations between any two ions:

$$\frac{N_{Z+a}}{N_Z} = \prod_{i=o}^{a-1} \frac{\alpha_{rZ+i}}{\alpha_{rZ+i} + \alpha_{dZ+i}} \qquad (3A)$$

$$\frac{N_{Z-b}}{N_Z} = \prod_{i=1}^{b} \frac{\alpha_{rZ-i} + \alpha_{dZ-i}}{\alpha_{rZ-i}} \qquad (4A)$$

If we wish to consider the ionization curve of Ca XV, we may obtain it from

$$\frac{N(\text{Ca XV})}{N} = \frac{N_{14}}{N} = \frac{N_{14}}{\sum_Z N_Z} = \left(\sum_Z \frac{N_Z}{N_{14}} \right)^{-1} \qquad (5A)$$

where the terms in the expansion (5A) are easily obtained from (3A) and (4A). In practice the terms in (5A) decrease rapidly on either side of the term $N_{Z=14}/N_{14} = 1$, so the abundance curve for any ion may be computed if the corresponding curves for ions two steps removed are known sufficiently accurately.

Using (5A) we computed the ionization curves of Ca XIV-XVI using relative abundances of Ca XII-XVIII for each ion. The results are shown in Fig. 10. Since we ignored all the ions more remote than Ca XII and Ca XVIII, the low temperature end of the Ca XIV curve and the high end of the Ca XVI curve may be in error somewhat -- of the order of a few percent. This is well within the range of possible errors introduced by the numerical approximations used for the ionization and recombination rates.

APPENDIX B - Sizes of Condensations

As a by-product of our investigation of the ionization in the yellow-line condensations, we obtained a rough estimate of the lengths of the condensations along the line of sight. From the line intensity ratios we determined the mean electron density along the line of sight. Since the condensations are taken to be optically thin, the total continuum brightness is proportional to the number of scattering electrons in the line of sight. Thus if L is the length of the condensation, N_e an average electron density in the condensation, and I(cont.) the intensity of the scattered continuum, then

$$L \cdot I(\text{cont.})/N_e \ . \qquad (1B)$$

For a process involving Thomson scattering, (1B) becomes (Zirin, 1964)

$$L = \frac{6.20 \times 10^{24}}{N_e} \frac{I(\text{cont.})}{I_\odot} \text{ cm} = \frac{6.20 \times 10^{4}}{N_e/10^{9}} \frac{I(\text{cont.})}{I_\odot} \times 10^{6} \text{ km.} \qquad (2B)$$

Table 3 shows for each spectrogram the measured line intensity ratio R, the electron density N_e, the continuum intensity I(cont.) in units of 10^{-6} times the photospheric intensity, and the resulting calculated lengths of the condensations, L. In two cases the results seem unreasonably large. The electron densities inferred are extremely sensitive to line ratio measurements, and the uncertainties in the latter (Section III) should be expected to produce sizeable errors. Also, we have no guarantee that all of the continuum in a given line of sight comes from the yellow-line region. In these cases rather dense, low-temperature material, as in a prominence loop, may be along the same line of sight. With these two exceptions, however, the calculated lengths all appear to be reasonable,

and a typical order of size may be considered to be around 20,000 km, or about .03 solar radii.

The authors wish to thank the staff of the High Altitude Observatory for the use of the spectrograms, and particularly David W. Dodgen, Keith Watson and Robert James, who recorded the spectra at the Climax Observing Station. Our thanks also go to Dr. R. H. Garstang for his help in obtaining the necessary oscillator strengths. This project was sponsored by the Office of Naval Research, grants Nonr-G 00059-64 and 00046-65.

CAPTIONS

Fig. 1. The first three levels of Ca XV.

Fig. 2. The variation of the fraction of Ca XV in the $^3P_1$ and $^3P_2$ states with electron density.

Fig. 3. The dependence of the ratio of the intensities of the two lines, λ5694 and λ5446 upon electron density.

Fig. 4. a). Microphotometer tracings of the two yellow coronal lines and the same spectral regions from a nearby quiet region of the solar limb. Note the absorption lines in the wings.

b). The profiles obtained from these two tracings by a measurement of $I - I_b$.

Fig. 5. The relation between line intensity ratio and line/continuum ratio as observed, in comparison with theoretical curves which assume a fixed value of F(Ca XV) = 0.2.

Fig. 6. Schematic representation of the method used to obtain values of F(Ca XV).

Fig. 7. A comparison of the values of F(Ca XV) calculated from the two lines for each condensation. Note the high correlation coefficient and tendency to a 45° slope.

Fig. 8. A plot of the calculated values of F(Ca XV) for each line against line width temperature and corresponding mean-square velocity. The comparison curve is obtained from ionization theory. The dotted-line extensions along the temperature axis represent the maximum possible error estimated from line half-width uncertainties.

Captions (Cont.)

Fig. 9. a). The measured increase of continuum emission in the condensations plotted against the difference in measured and theoretical temperatures, and corresponding mean-square velocities, using method (1) as given in the text.

b). The same plot using method (2).

Fig. 10. The ionization curves of Ca XIV, XV, and XVI.

TABLE 1

Date	Time UT	I/I_{cont} 5694	I/I_{cont} 5446	$N_e/10^9$	$F(^3P_1)$	$F(^3P_2)$	F(CaXV) 5694	F(CaXV) 5446	$T/10^6$ 5694	$T/10^6$ 5446
9/III/56	1950	4.17	2.27	9.1	.097	.062	.34	.29	4.37	
12/XI/56	1634	1.73	0.73	4.0	.055	.031	.28	.19	3.63	6.14
12/XI/56	1720	3.16	2.03	27	.184	.138	.14	.12	6.29	
12/XI/56	1729	2.10	0.46						5.52	
12/XI/56	2005	4.62	3.61	90	.296	.253	.12	.14	8.59	7.25
12/XI/56	2006	5.45	4.22	88	.292	.249	.15	.14	5.68	4.86
12/XI/56	2007	4.13	3.69						5.63	6.24
14/XII/57	1734	2.43	1.25	7.4	.081	.050	.24	.20	5.83	7.45
9/VI/59	2141	2.50	1.28	7.4	.081	.050	.25	.20	4.47	
20/XI/60	2227I	2.08	1.38	33	.202	.155	.082	.071	4.77	5.38
20/XI/60	2227IIa	2.59	1.78	42	.225	.178	.092	.080	6.54	3.96
20/XI/60	2227IIb	2.37	1.28	9.0	.095	.060	.20	.17	5.23	4.23
20/XI/60	2227IIc	2.54	2.01	105	.307	.269	.066	.060	4.31	5.51

TABLE 2

Date	Time UT	$\Delta T_1/10^{6\circ}$K		$\Delta T_2/10^{6\circ}$K		$\Delta\lambda$ (Å)	
		5194	5446	5694	5446	5694	5446
9/III/56	1950	1.1		1.1		.03	
12/XI/56	1634	0.3	2.5	0.3	2.5	.17	.09
12/XI/56	1720	2.4		2.4		.15	
12/XI/56	1729					.17	
12/XI/56	2005	4.6	3.3	4.6	3.3	.12	.05
12/XI/56	2006	1.8	1.0	1.8	2.1	.00	.04
12/XI/56	2007					.17	.11
14/XII/57	1734	2.4	3.8	2.7	3.8	.12	.11
9/VI/59	2141	1.2		1.2		.11	
20/XI/60	2227I	0.6	1.1	2.2	1.1	.13	.10
20/XI/60	2227IIa	2.4	1.3	2.4	1.3	.36	.06
20/XI/60	2227IIb	1.6	0.5	2.2	1.4	.08	.24
20/XI/60	2227IIc	0.0	1.1	1.8	1.1	.03	.23

TABLE 3

Date	Time UT	R	$N_e/10^9$	$\frac{I(cont.)}{I_\odot} \times 10^6$	L(km)
9/III/56	1950	1.84	9.1	2.16	14,700
12/XI/56	1634	2.38	4.0	16.6	258,000
12/XI/56	1720	1.55	27	5.46	12,500
12/XI/56	1729	4.58		5.46	
12/XI/56	2005	1.28	90	8.51	5,860
12/XI/56	2006	1.29	88	9.53	6,710
12/XI/56	2007	1.12		13.8	
14/XII/57	1734	1.95	7.4	9.47	79,300
9/VI/59	2141	1.95	7.4	8.19	68,600
20/XI/60	2227I	1.51	33	25.2	47,400
20/XI/60	2227IIa	1.45	42	18.6	27,500
20/XI/60	2227IIb	1.85	9.0		128,000
20/XI/60	2227IIc	1.26	105		11,000

REFERENCES

Allen, C. W. 1965, Space Science Reviews, 4, 91.

Billings, D. E. 1963, Ap. J., 137, 592.

Blaha, M. 1962, Bul. Astr. Inst. Czech., 13, 81.

Boardman, W. J., and Billings, D. E. 1965, Ap. J., 141, 1289.

Burgess, A. 1965, Ap. J., 141, 1588.

Burgess, A., and Seaton, M. J. 1964, M. N., 127, 335.

Lüst, R., and Zirin, H. 1960, Zs. f. Ap., 49, 8.

Pecker, C., Billings, D. E., and Roberts, W. O. 1954, Ap. J., 120, 509.

Roberts, Walter Orr 1952, Ap. J., 115, 488.

Seaton, M. J. 1962, Observatory, 82, 111.

Seaton, M. J. 1964, Plan. Space Sci., 12, 55.

Shklovsky, I. S. 1950, Izv. Krymsk. Ap. Obs., 5, 109.

van de Hulst, H. C. 1953, "The Chromosphere and the Corona", The Sun, Ch. 5, ed. Kuiper, 207.

Varsavsky, C. M. 1961, Ap. J. Suppl., 6, 75.

Waldmeier, M. 1951, Zs. f. Ap., 29, 29.

Waldmeier, M. 1956, Zs. f. Ap., 39, 219.

Woolley, R. v. d. R., and Allen, C. W. 1948, M. N., 108, 292.

Zirin, H. 1959, Ap. J., 129, 414.

Zirin, H. 1964, Ap. J., 140, 1216.

Fig 1

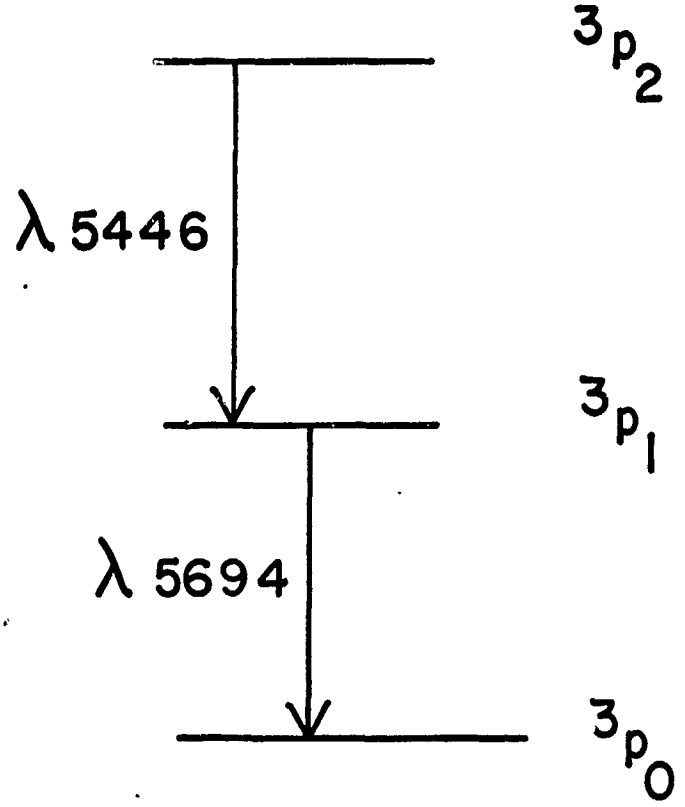

Fig 2

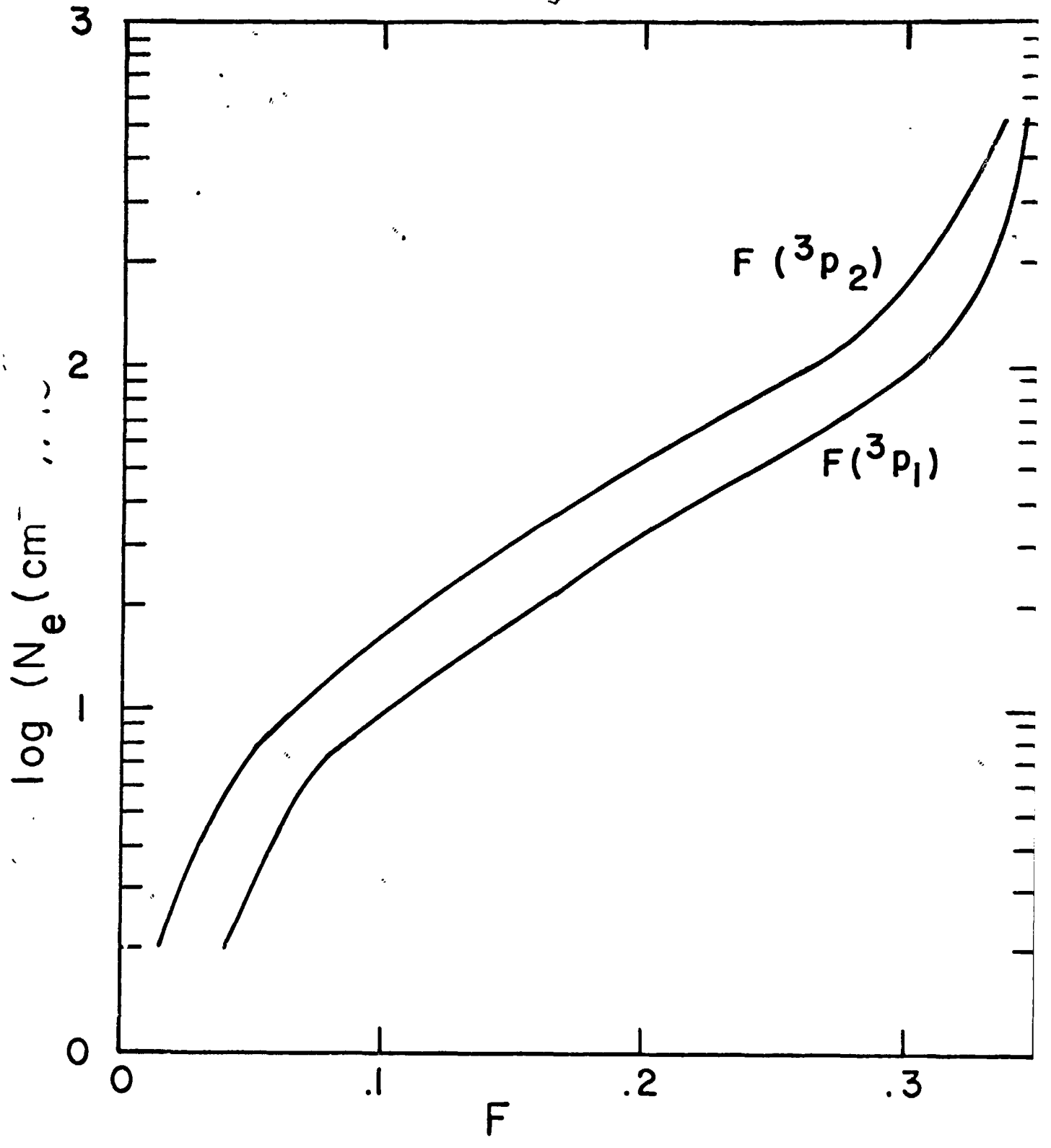

Fig 3

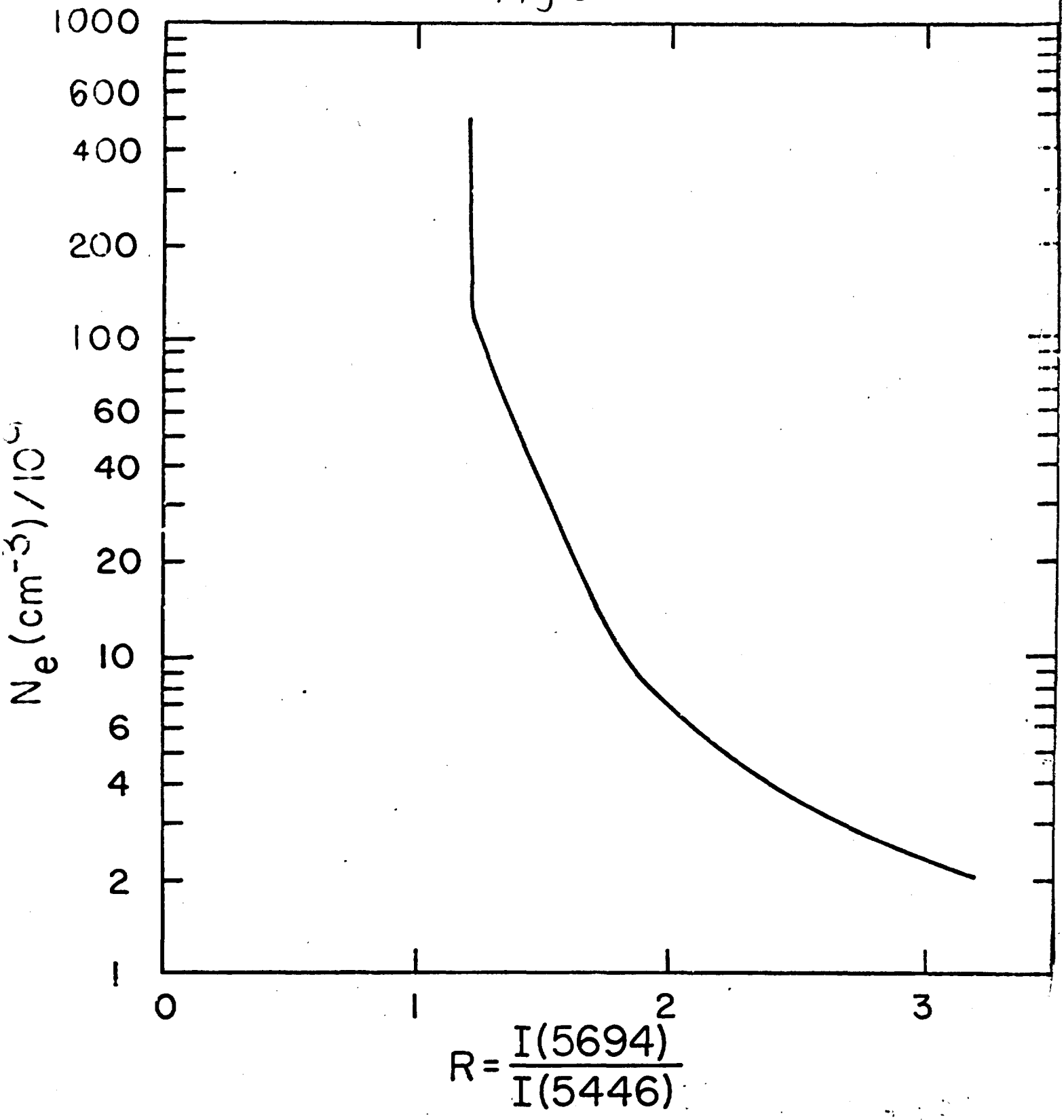
1000
600
400
200
100
60
40
20
10
6
4
2
1
$N_e\,(cm^{-3})/10^5$
0
1
2
3
$R = \frac{I(5694)}{I(5446)}$

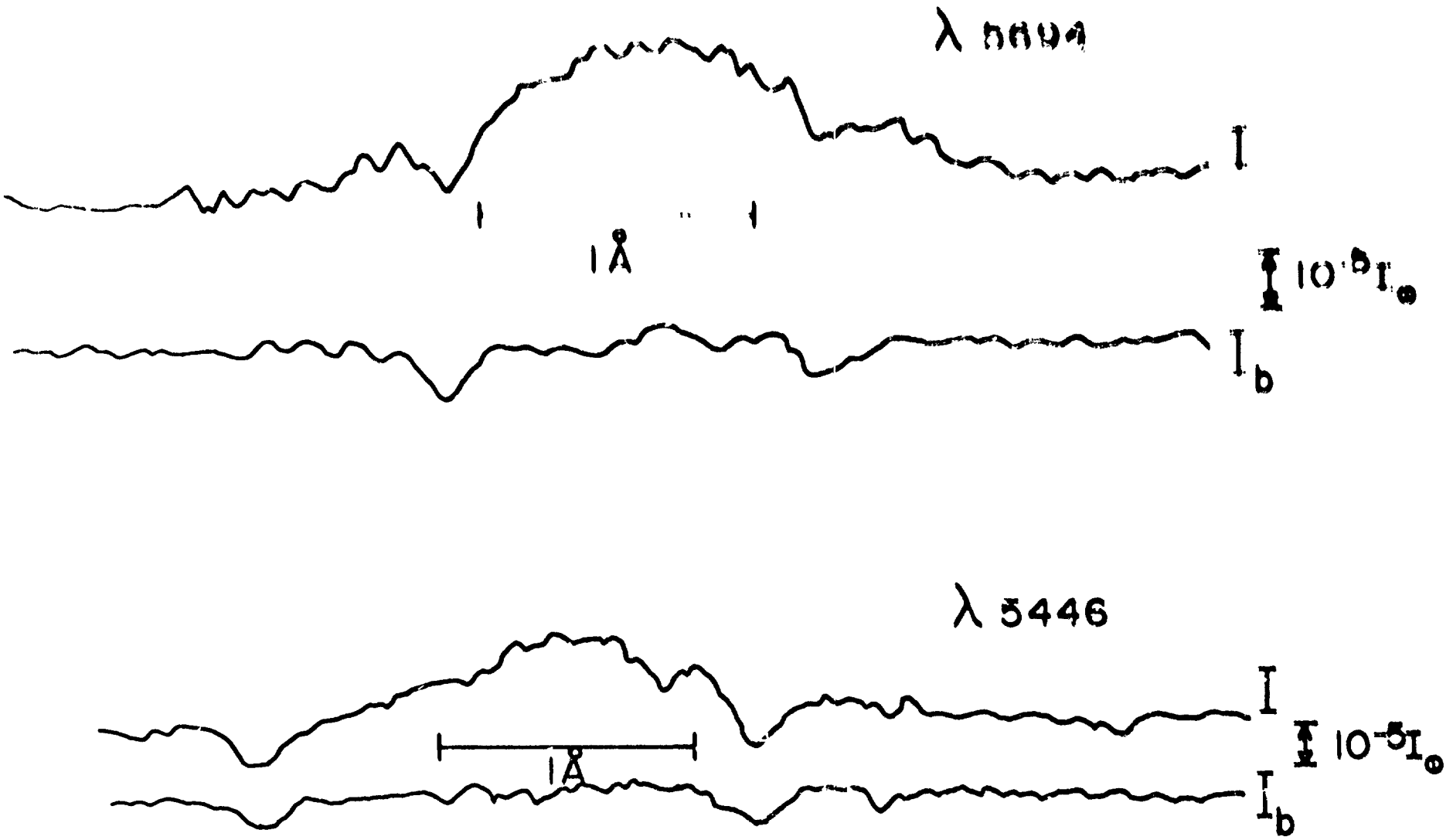
λ 5434
I
1Å
$10^{-5}I_\odot$
I_b
λ 5446
I
$10^{-5}I_\odot$
1Å
I_b

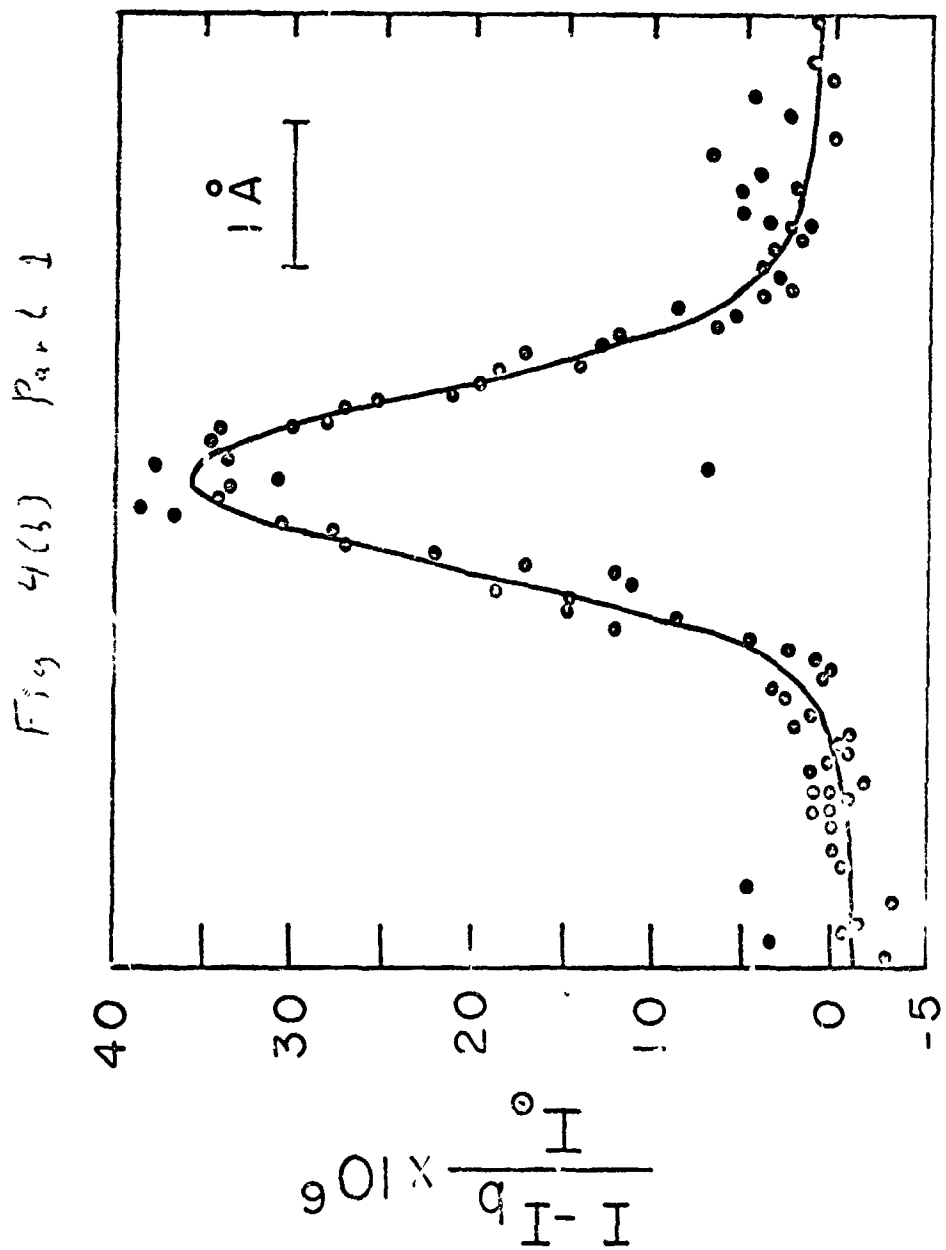

Fig 4(b) Panel 1

Fig 4(b) Part 2

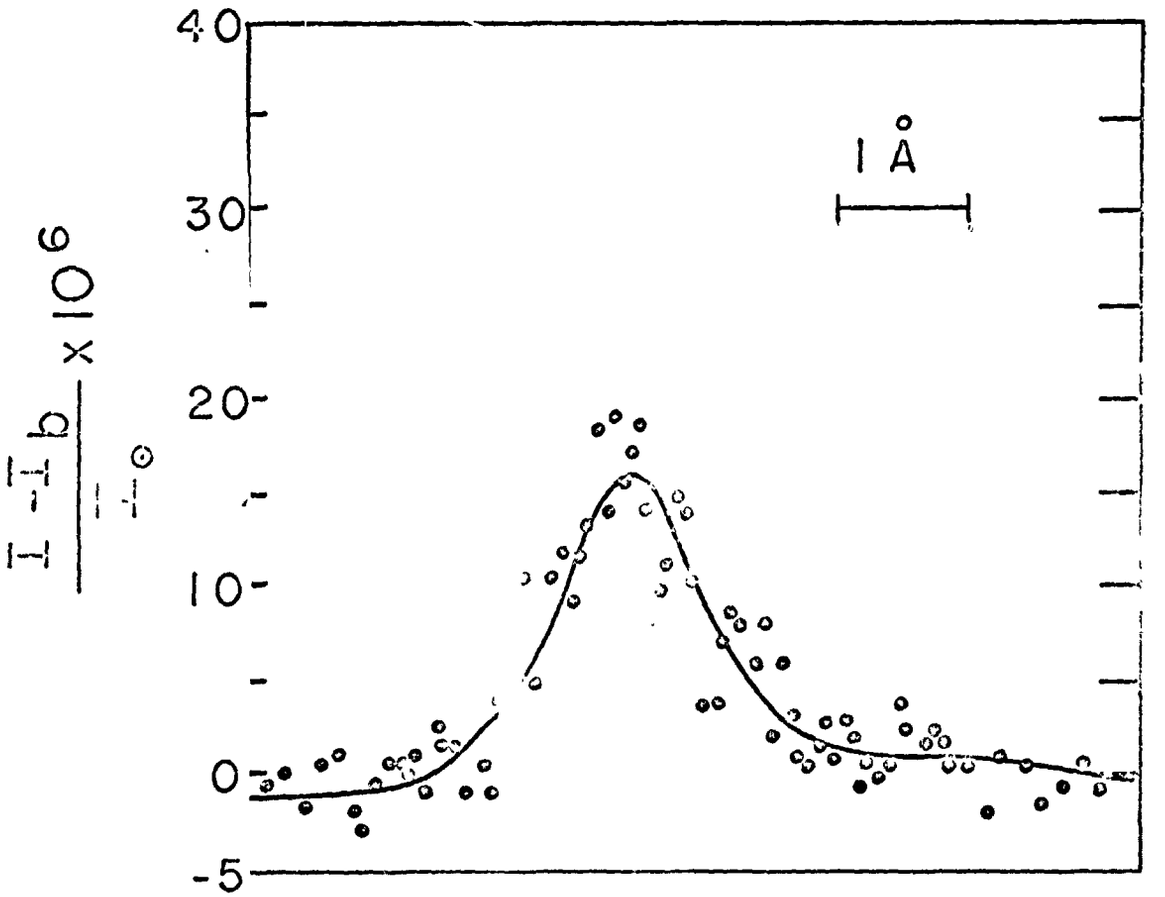

Fig. 5

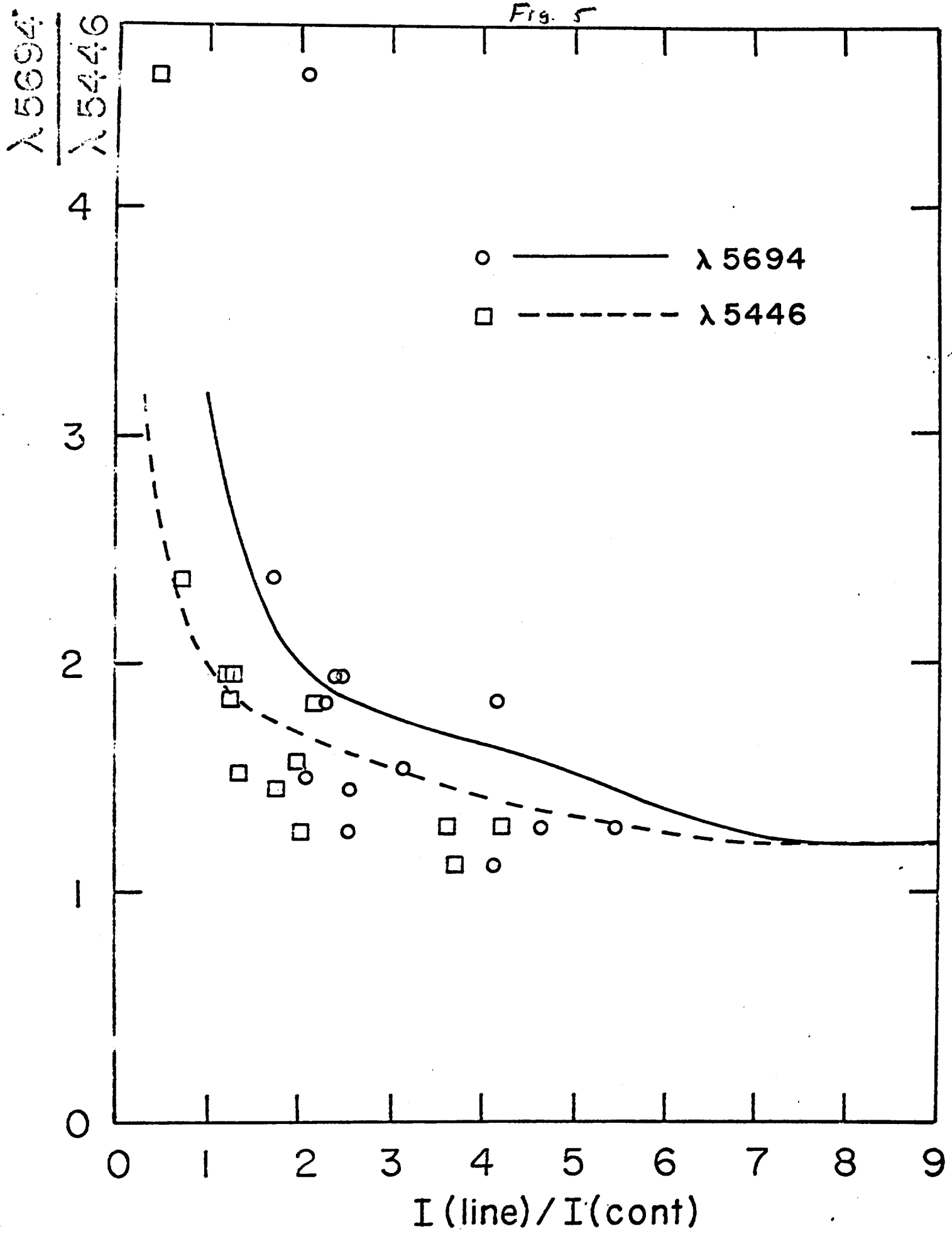

Fig. 6

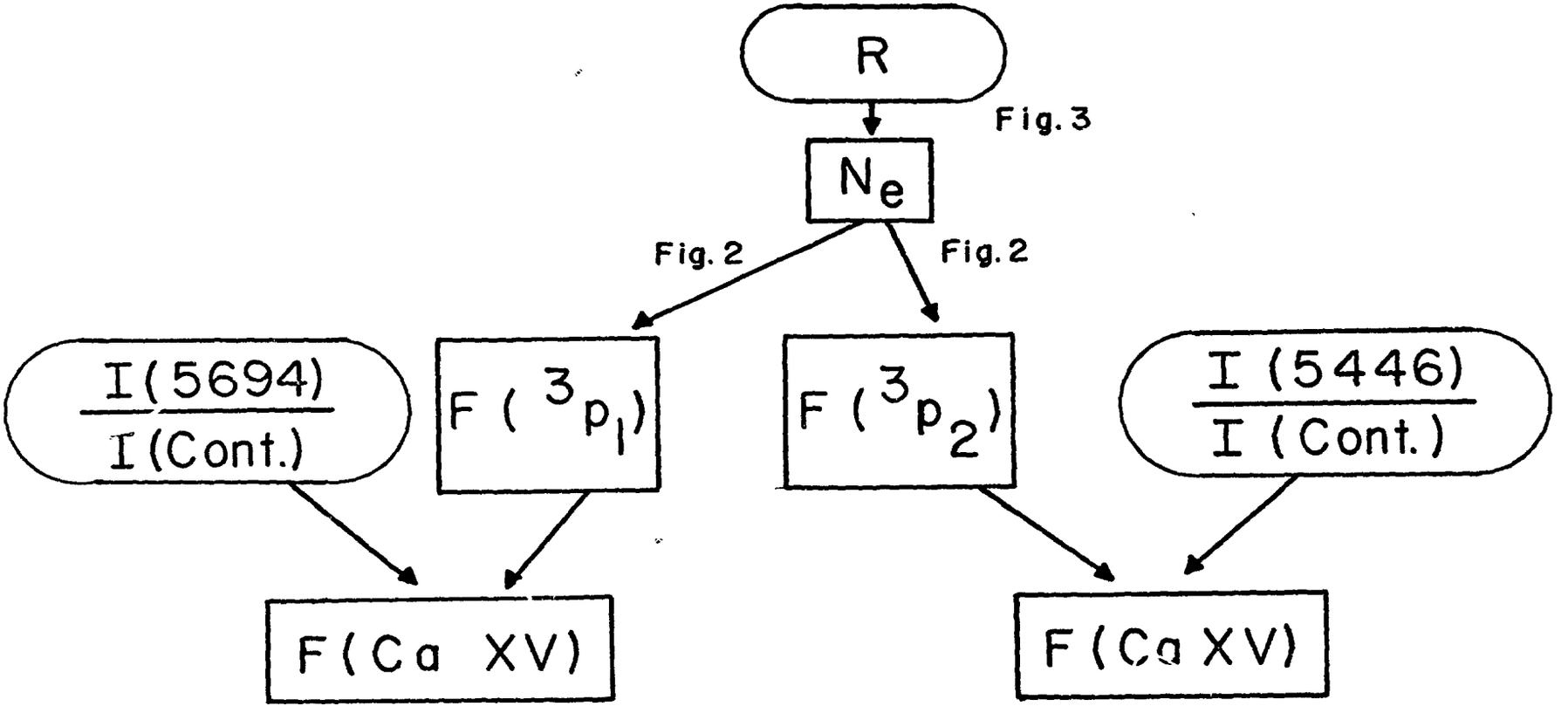

310

fig 6

Fig. 7

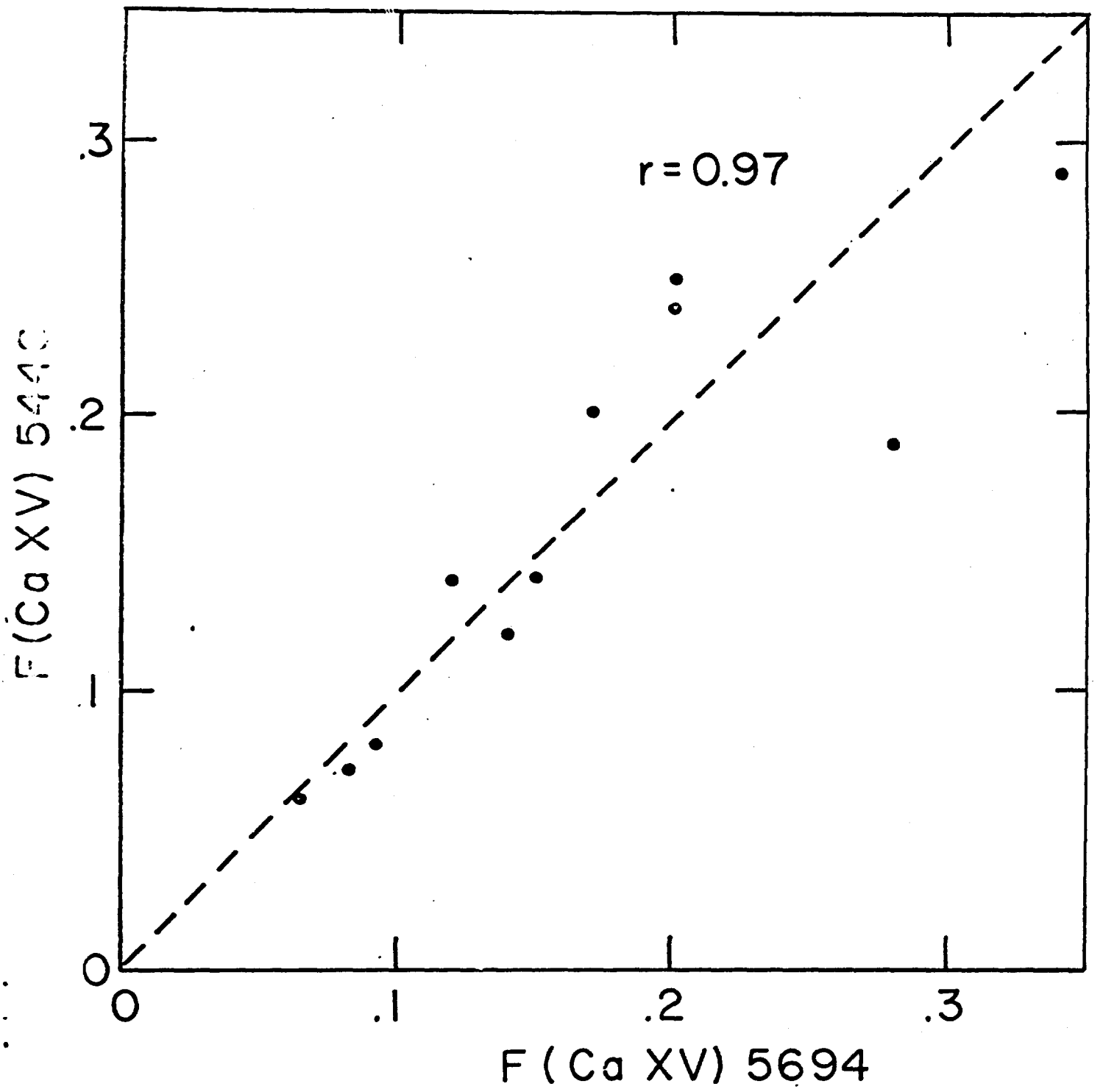

f.7(7)

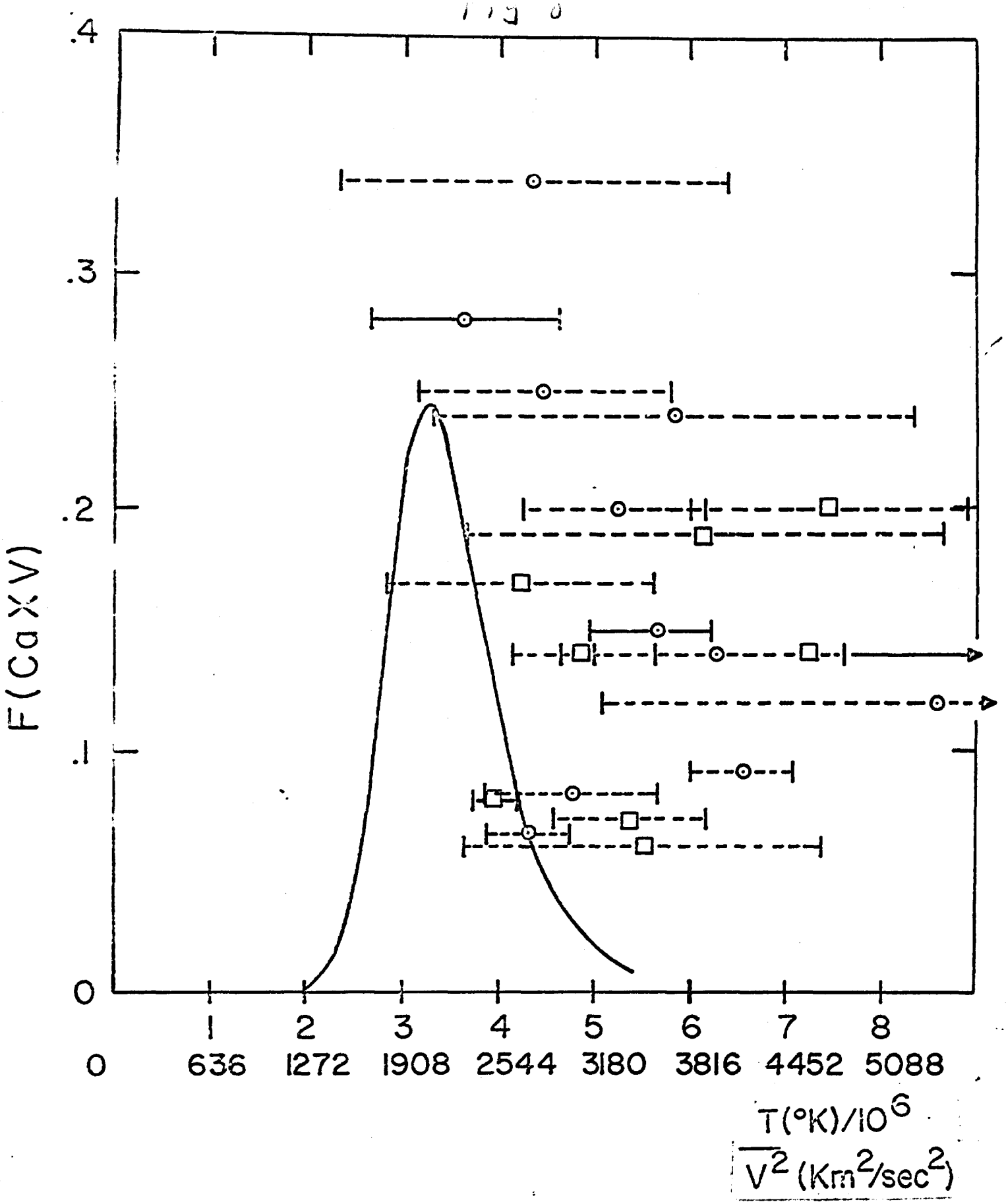
.4
.3
.2
.1
0
F(CaXV)
1
2
3
4
5
6
7
8
0
636
1272
1908
2544
3180
3816
4452
5088
T(°K)/10^6
V^2 (Km^2/sec^2)

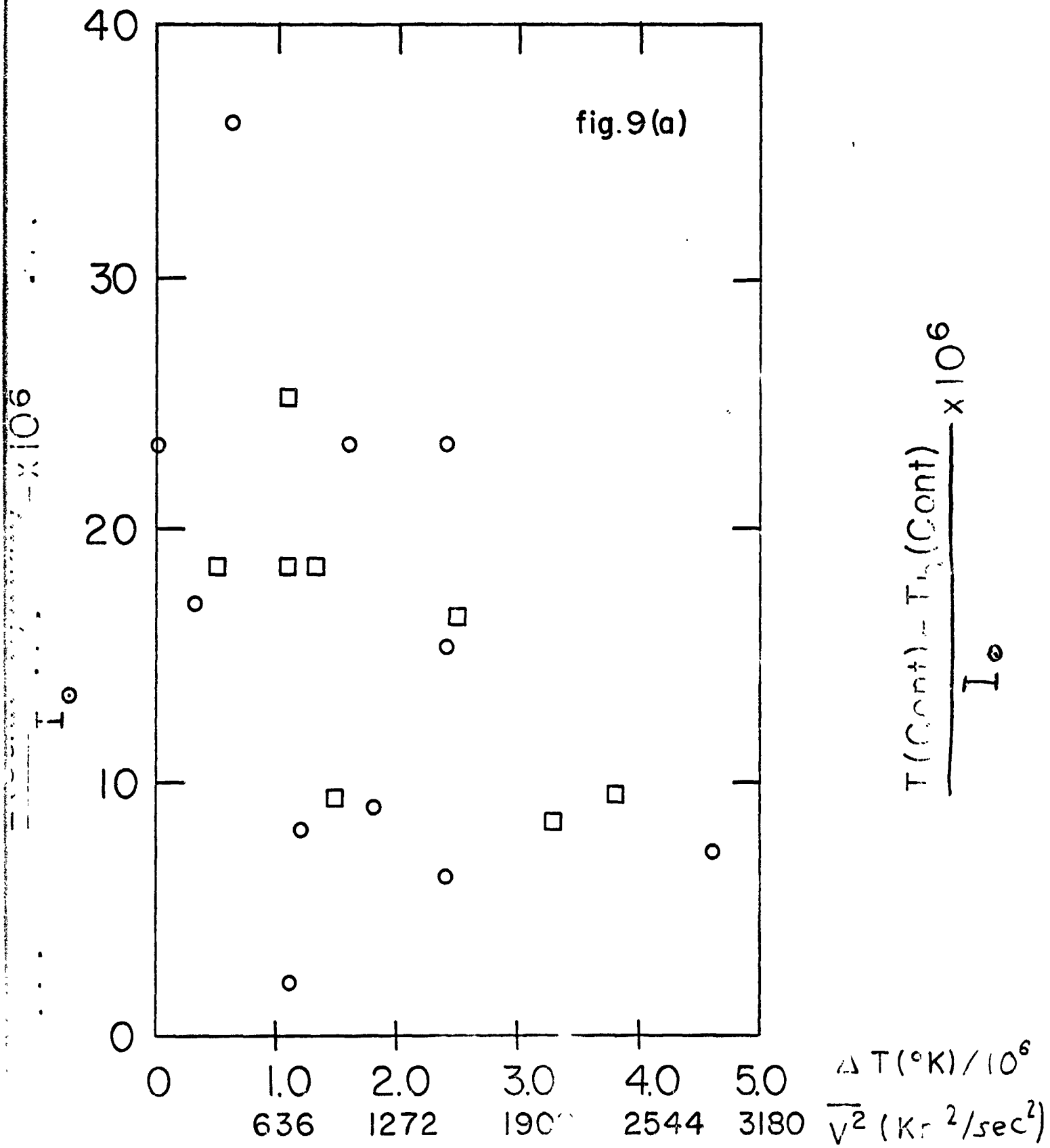
fig.9(a)
40
30
20
10
0
0
1.0
2.0
3.0
4.0
5.0
636
1272
1900
2544
3180
$\Delta T(°K)/10^6$
$\overline{V^2}$ (Kt^2/sec^2)
$\frac{T(Cont) - T_h(Cont)}{T_\odot} \times 10^6$
$\frac{T(Cont) - T_h(Cont)}{T_\odot} \times 10^6$
$T_\odot$

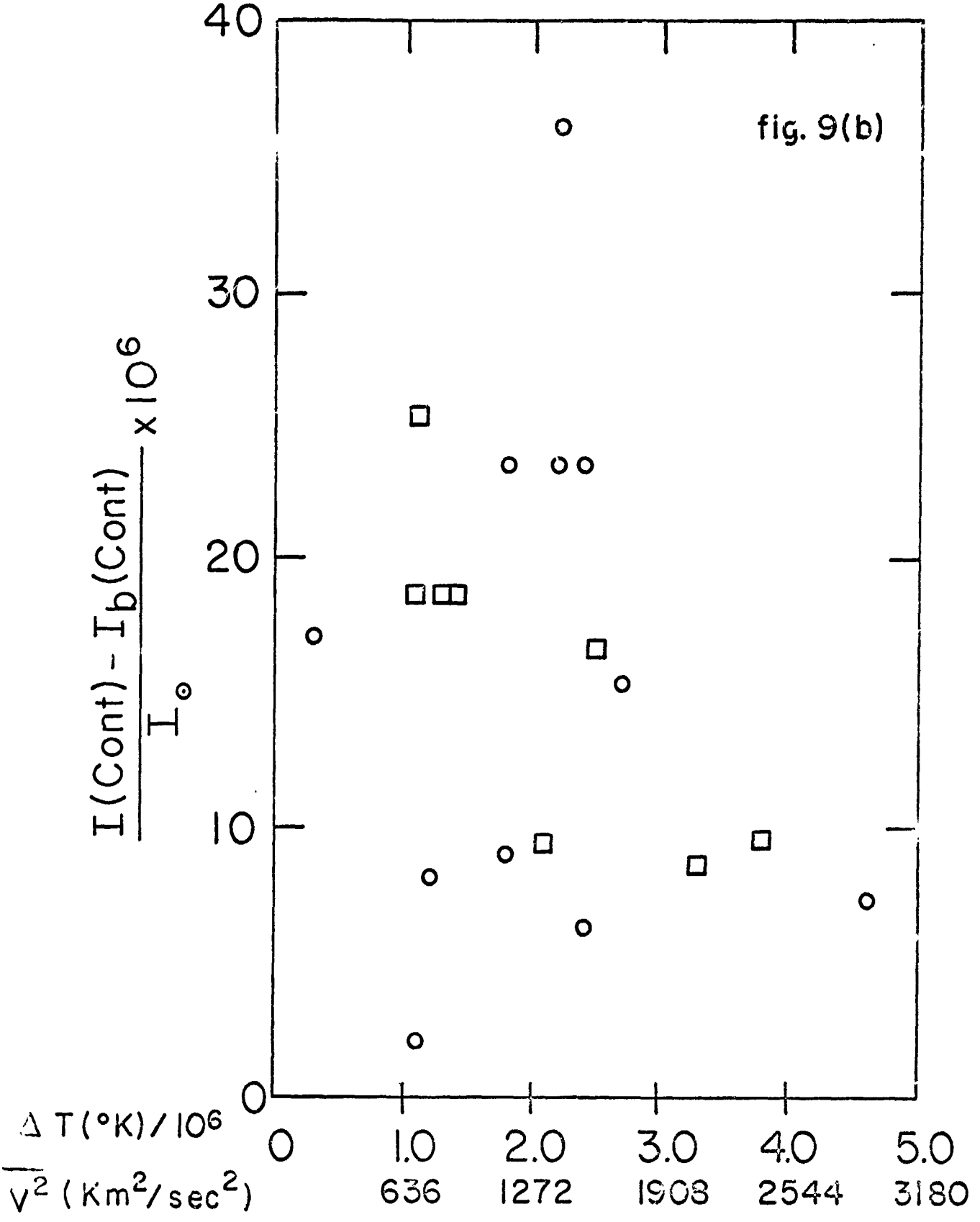
fig. 9(b)
40
30
20
10
0
$\frac{I(Cont) - I_b(Cont)}{I_\odot} \times 10^6$
$\Delta T(°K)/10^6$
$\overline{V^2}$ (Km^2/sec^2)
0
1.0
636
2.0
1272
3.0
1908
4.0
2544
5.0
3180

Fig. 10